communications physics

Article

https://doi.org/10.1038/s42005-024-01903-3

Next-generation neutron detection using a ^{6}Li glass scintillator composite

Andrea Favalli[1,2] ✉, Brenden W. Wiggins[1], Metodi Iliev[1], Cameron G. Richards[1], Kristofer Ogren[1], Thomas D. McLean[1], Kiril D. Ianakiev[1] & Markus P. Hehlen[1] ✉

Neutron detectors are crucial in fundamental science, nuclear security, safeguards, and civil applications. ^{3}He-filled gas proportional counters are the gold standard for thermal neutron detection, prized for their efficiency, neutron/gamma discrimination, and stability; however, the scarcity of ^{3}He has prompted the search for alternatives. Here, we introduce a neutron detector design based on a scintillating composite consisting of ^{6}Li glass scintillator particles dispersed in an organic matrix. A detector consisting of this scintillating composite, photomultiplier tubes (PMTs) for optical detection, and electronics for reading out the PMT signal in both pulse and current modes was prototyped and characterized using various neutron and gamma sources. The prototype achieves a measured intrinsic detection efficiency of 6.70 ± 0.01%, a die-away time of 10.3 ± 0.1 μs, a negligible gamma misidentification probability, and response linearity up to at least 3.7 × 10^{6} incident neutrons/s established via a cross-calibration technique. This detector holds the potential to outperform traditional ^{3}He-gas-based neutron detection systems, offering a viable alternative amidst the ongoing ^{3}He shortage and promising advancements in neutron detection technology.

Detecting neutrons amidst ubiquitous gamma-ray backgrounds is crucial in various scientific fields, including nuclear physics, neutron scattering science, fusion research, nuclear safeguards, security, nuclear engineering, and industrial well-logging applications[1–6]. Because of their neutral charge, neutrons do not produce ionization when passing through a material and instead interact primarily with atomic nuclei through scattering or nuclear reactions. As a result, direct detection via their induced charge, as is the case for alpha or beta particles, is not feasible for neutrons. Instead, neutron detection hinges on ionization by secondary particles, such as recoiling nuclei (protons) or charged reaction products. The principal mechanism for neutron detection also depends on the energy of the incident neutrons. "Fast" neutrons, which have energies on the keV to MeV scale, interact primarily through scattering on atomic nuclei, and the ionization induced by the recoiling nucleus can be used as the means for detection. Materials containing hydrogen are preferred for this application. Neutrons produced in nuclear fission are an example of fast neutrons. For lower energy "slow" neutrons (less than a few eV), most detection methods rely on nuclear reactions that become more probable at low energy, such as neutron capture. Some key isotopes, such as ^{3}He, ^{6}Li, and ^{10}B, have relatively high neutron capture cross-sections for thermal neutrons (~ 25 meV). These reactions release a substantial amount of energy (hundreds of keV to a few MeV) in the form of charged particles, making them relatively easy to detect[2–5].

Neutron detectors based on ^{3}He gas proportional counters have traditionally been considered the gold standard for thermal neutron detection. In such detectors, an incident neutron, usually first thermalized in a moderator material such as polyethylene, interacts with the ^{3}He gas via the ^{3}He(n,p)^{3}H neutron capture reaction, which has a large thermal neutron cross-section (5330 barns[4]). The charge impulses induced by the p and ^{3}H interactions into the gas are then converted to logic pulses. Gamma rays, on the other hand, interact only weakly with the ^{3}He gas. When the voltage pulses are viewed in a pulse-height spectrum, neutron capture produces significantly greater pulse heights than gamma interactions, and neutrons can thus be detected reliably as events having a pulse height greater than a pre-set threshold. These detectors offer excellent performance, such as high neutron detection efficiency, effective neutron/gamma discrimination, and long-term stability, making them the most widely deployed type of neutron detector[4,5]. According to A. Cho[7] and F. Sacchetti et al.[8], 84.5% of the usage of ^{3}He gas in neutron detectors is dedicated to security applications, followed by neutron scattering and scientific applications (10%).

The potential for special nuclear material (SNM) to be lost, diverted, or misused in the civil nuclear fuel cycle is a significant concern for the international community. To address this concern, portal monitors, portable neutron detectors, and neutron well counters are commonly used detector systems in nuclear security, non-proliferation, and safeguards to detect potential nuclear material diversion for clandestine purposes.

[1]Los Alamos National Laboratory, Los Alamos, P.O. Box 1663 Los Alamos, NM, 87545, USA. [2]European Commission, Joint Research Centre (JRC), I-21027 Ispra, Italy. ✉e-mail: andrea.favalli@ec.europa.eu; hehlen@lanl.gov

Another common application of ^{3}He detectors is neutron multiplicity measurements for nuclear material control and accounting (NMC&A). Conventional passive neutron multiplicity counting (PNMC), using a thermal neutron well-counter, is a well-established method for assaying special nuclear materials like plutonium. In this technique, an item is placed inside a well-counter comprised of numerous (dozens to more than a hundred) ^{3}He proportional counters embedded in high-density polyethylene, with ^{3}He gas pressure ranging from 4 to 10 atm. The charge impulses collected from the ^{3}He proportional detectors are converted into logic pulses and summed together to create the pulse train. In PNMC, the first three factorial moments of the neutron detected triggered count-rate histogram are extracted from the pulse train. They are called Singles, Doubles (correlated pairs), and Triples (correlated triplets); they are related to the properties of the special nuclear material under assay. The conventional ^{3}He-based design has enabled the construction of thermal-neutron well counters with high neutron detection efficiency, defined as counts per neutron emitted from the measurement item, with efficiencies up to about 50–60% for fission neutrons when an item is located in the center of the cavity. It is worth noting that in Doubles counting, the efficiency increases with the square of the efficiency of the detector, and in Triples counting, it increases with the cube of the efficiency, making the efficiency a demanding property of a multiplicity detector system. The ^{3}He-based systems offer a relatively short detector time response, so-called die-away (some 10 s of μs), as a short die-away time allows to minimize accidental coincidences[5,9,10]. Neutron/gamma separation, efficiency, short die-away, and long-term stability are critical requirements for this application. In recent decades, the limited supply and high cost of ^{3}He have spurred extensive research into alternative neutron detection technologies. Exploring alternative techniques for neutron multiplicity counting – one of the more demanding neutron detection techniques described above – presents unique challenges[11–19].

The present study focuses on developing a neutron detector as a viable alternative to ^{3}He-based neutron detectors. The detector presented here is based on scintillating composites, wherein ^{6}Li-enriched glass scintillator particles serve as neutron detection centers in a non-scintillating matrix. The matrix acts as both a moderator and a light collector. The size and distribution of the glass particles governs the gamma sensitivity. Our focus is primarily on nuclear safeguards and security applications, such as neutron multiplicity counting. Similar to ^{3}He, ^{6}Li has a sizeable thermal neutron capture cross-section (940 barns) via the ^{6}Li(n,α)^{3}H reaction (reaction Q-value = 4.78 MeV: ^{3}H at 2.73 MeV, and α at 2.05 MeV)[20]. In contrast to ^{3}He, the ^{6}Li$^+$ ion can be a high atom density constituent of solid scintillators, allowing sizeable neutron capture cross-sections to be realized. Furthermore, ^{6}Li is much more readily sourced than ^{3}He and can thus be a potential alternative for efficient neutron capture. The neutron detector developed in this work utilizes scintillating composites consisting of small ^{6}Li glass scintillator cubes (GS20^{TM}, Scintacor, Cambridge, UK; 95% ^{6}Li enriched, 6.6 wt% ^{6}Li[21]) of 1.5 mm × 1.5 mm × 1.5 mm in size that are dispersed in a non-scintillating optically transparent mineral oil matrix at a density of 2.8 vol%[17]. Incident fast neutrons, such as fission neutrons, are moderated to thermal energies within the organic matrix and subsequently captured by ^{6}Li in the ^{6}Li glass scintillator cubes, where they convert to charged particles through the ^{6}Li(n,α)^{3}H reaction. These reaction products deposit their energy in the ^{6}Li glass matrix, a portion of which excites the Ce^{3+} dopant, which subsequently decays to the ground state via the 5 $d \rightarrow 4f$ optical transition around 395 nm (57 ns lifetime). Through this process, ~6,000 optical photons are emitted isotropically per neutron capture event[17,21]. This scintillation light then propagates through the optically transparent mineral oil matrix to photodetectors that are optically coupled to the composite. In contrast, the secondary electrons ejected by gamma-ray interactions within the ^{6}Li glass scintillator and the mineral oil only deposit relatively small amounts of energy in the small scintillator particles, most of these electrons passing through the scintillator cube, producing significantly fewer photons than the scintillation from a single neutron capture event. As we will show, this enables excellent neutron/gamma discrimination via simple pulse-height discrimination akin to ^{3}He gas proportional counters (see Fig. 1)[16–18]. An initial computational investigation provided directions on the design parameters (particle size, spacing between scintillator

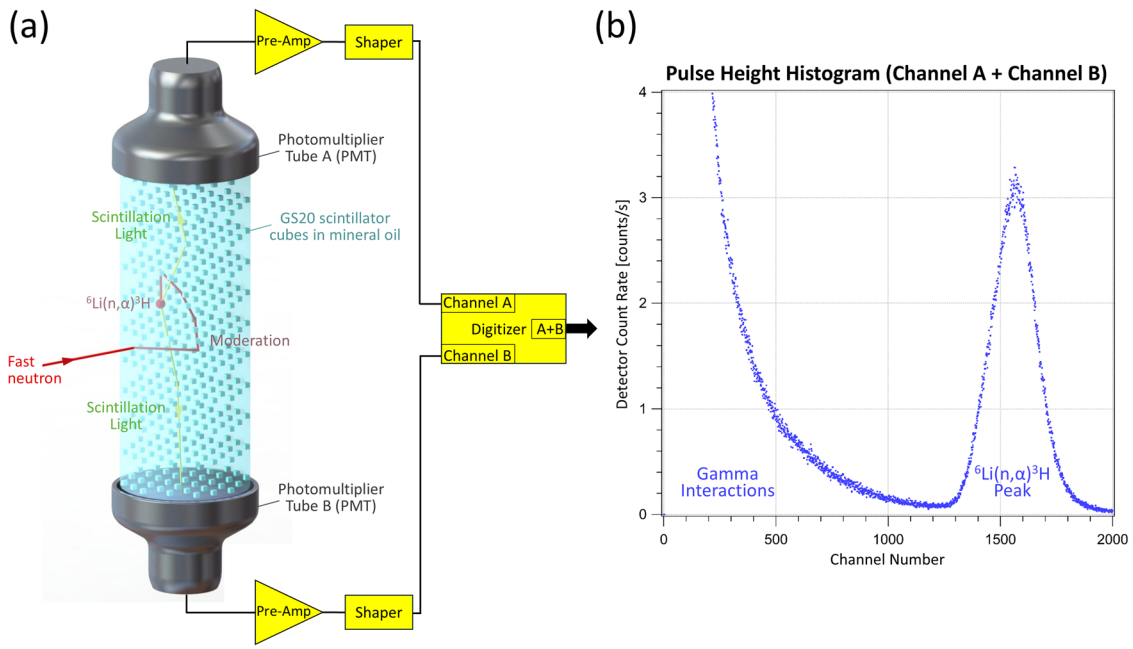

Fig. 1 | Schematic illustration of the operating principle of the ^{6}Li-glass scintillator composite neutron detector. a Fast incident neutrons (red arrow) are moderated within the matrix consisting of ^{6}Li glass (GS20^{TM}) particles suspended in mineral oil, where they undergo capture in the ^{6}Li glass particle through the ^{6}Li(n,α)^{3}H nuclear reaction. Subsequently, the reaction products produce scintillation light within the ^{6}Li glass particle, which propagates (green arrows) to the two photomultipliers (PMT) for detection. Electric signals from the PMTs are pre-amplified and shaped, followed by digitization and summing. **b** The summed signals are sorted in a multichannel analyzer to produce a pulse height histogram. The channel number is proportional to pulse height. In this pulse-height spectrum, the ^{6}Li neutron capture peak is evident and well separated from the low amplitude signal due to gamma interactions.

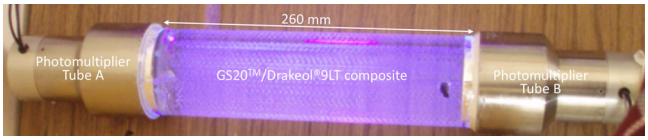

Fig. 2 | Image of the full prototype equipped with two photomultiplier tubes. Here, the ^{6}Li glass scintillator composite is seen luminescing in a purple color under the illumination with ultraviolent light (optical excitation of Ce^{3+} in the ^{6}Li glass scintillator). The cadmium sheet and the optical reflector surrounding the tube containing the ^{6}Li glass (GS20™)/mineral oil (Drakeol®9LT) composite were removed for this picture. The length of the cylindrical composite is shown for scale.

particles) to minimize gamma misidentification while maintaining high neutron detection efficiency[18].

In the following sections, we present a comprehensive analysis of the neutron detection properties of the ^{6}Li glass composite scintillator detector described above. This detector system showcases excellent capabilities: excellent neutron/gamma discrimination, a short die-away time, and a detection efficiency that is comparable or superior to traditional ^{3}He detectors embedded in high-density polyethylene moderators are demonstrated. These properties are particularly favorable for the future construction of thermal neutron multiplicity counters with performance and attractive cost compared to the current ^{3}He-based neutron multiplicity counting systems. Additionally, we assess the performance of this ^{6}Li glass composite scintillator detector under exposure to a high-intensity ^{252}Cf spontaneous fission neutron source. The results indicate that the ^{6}Li glass composite scintillator detector significantly surpasses the performance of the ^{3}He-based detector system, presenting an attractive alternative for a range of neutron detection applications in which high neutron fluxes (continuous or pulsed) are present.

Results

The fabrication process of the scintillating composite neutron detector is described in the Methods section (see Detector Fabrication). The detector consisted of 8200 cubes of GS20™ (Scintacor, Cambridge, UK) ^{6}Li glass scintillator, each 1.5 mm × 1.5 mm × 1.5 mm in size and attached to fused silica rods. These assemblies were then immersed in mineral oil inside a 69.7 mm diameter by 260 mm long fused silica tube. Hamamatsu R6233 photomultiplier tubes were glued to each end of the fused silica tube. The fused silica tube was wrapped with an optical reflector and finally with a 0.5 mm thick sheet of cadmium. Figure 2 shows a picture of the detector.

Detector performance evaluation

Pulse-height spectra. First, the pulse-height spectrum of the natural background radiation at Los Alamos National Laboratory (2198 m above sea level) was measured without any test source present (see Fig. 3a). This background spectrum was then subtracted from the raw spectra measured with sources present. The detector was exposed to a 10.5 μCi ^{252}Cf fast fission neutron source, as well as to ^{137}Cs, ^{60}Co, and ^{232}Th gamma sources to determine the gamma/neutron separation in the pulse-height spectrum and the associated gamma misidentification probability. Figure 3b shows the pulse-height spectrum for exposure to the ^{252}Cf source. The pulse-height spectrum comprises a peak centered around channel 1560 that is due to neutron capture events on ^{6}Li followed by Ce^{3+} scintillation emission as well as a broad distribution at lower channel numbers that is due to gamma-ray interactions and some neutron capture events that did not deposit their full energy because the reaction products escaped the scintillator particle. A Gaussian fit to the neutron capture peak (solid orange curve in Fig. 3b) indicates an energy resolution (defined as full width at half maximum (FWHM) relative to the peak centroid) of 15.3% with a centroid at channel 1560. The intersection of the Gaussian fit to the neutron capture peak and the gamma distribution was determined to be at channel 1310. As a result, the region of interest (ROI), defining neutron capture events, was set from channel 1310 to 2000 (the highest channel recorded in the multi-channel analyzer) for the measurements.

Figure 3c shows the pulse-height spectra due to pure gamma-ray sources in comparison with the neutron distribution measured above. The emission energies of the gamma source used here are 662 keV (^{137}Cs), 1173 and 1333 keV (^{60}Co), and 2614 keV (^{232}Th). Notably, ^{137}Cs is a significant contributor to the gamma emission from irradiated nuclear fuel, given its half-life of approximately 30 years[5,22].

The excellent separation in pulse height between neutron and gamma events observed in Fig. 3 is a direct result of the structure of the ^{6}Li glass composite scintillator. The ranges of the ^{3}H and α produced by a neutron capture reaction on ^{6}Li are small compared to the ^{6}Li glass scintillator cube dimensions. On average, ^{3}H and α deposit nearly all their energy into the glass host, where part of it is converted to scintillation photons. In contrast, gamma rays only deposit a small fraction of their energy into the ^{6}Li glass scintillator cubes, resulting in a significantly smaller number of scintillation photons and, thus, a smaller detected pulse height when compared to neutron capture events. Neutrons could, therefore, be detected with high confidence by setting a pulse height threshold at channel 1310 (see Fig. 3b) and counting events with pulse heights greater than this threshold.

To evaluate the probability of misidentifying a gamma event as a neutron event, we define the gamma misidentification probability as the fraction of the gamma distribution present in the ROI chosen for the neutron capture peak (channels 1310–2000), which is indicated by the dashed blue vertical line in Fig. 3c. Although the pulse-height spectra were corrected for background, the statistics achieved during the background spectrum acquisition time (49089 s) was insufficient for the ^{137}Cs and ^{60}Co spectra to converge to their actual values in the ROI. Instead, the Compton tails of the ^{137}Cs, ^{60}Co, and ^{232}Th spectra were fitted by double-exponential functions to obtain better representations of the respective gamma contributions in the ROI. From these fits, we find a gamma misidentification probability of 9.41×10^{-3} for ^{232}Th. In contrast, for ^{137}Cs and ^{60}Co, the Compton edges drop off well below the ROI, and the respective gamma misidentification probabilities are close to zero.

Note that, given the position and width of the neutron capture peak relative to the gamma distribution in the pulse-height spectrum, there is ample room to further reduce the gamma misidentification probability by increasing the pulse-height threshold, i.e. increasing the lower channel bound of the ROI. This would be particularly effective for ^{232}Th, which emits several gamma rays with high energy. The tradeoff of increasing the pulse-height threshold is that some neutron capture events will then not be counted. The choice depends on the needs of the application. The gamma misidentification probabilities given above should, therefore, be viewed as upper limits.

Neutron/Gamma discrimination stability to variation of high voltages. Measurements were conducted to evaluate the sensitivity of the neutron counts to variations in the high voltages (HV) applied to the photomultipliers (PMTs). For this purpose, the variation of the combined ROI count rate was measured for different PMT A and PMT B high voltage settings with the detector exposed uniformly to a ^{252}Cf neutron source. The individual ROI count rates were initially matched by setting PMT A to 1000 V and adjusting PMT B to 983 V, and then the resulting combined ROI count rate served as the reference (shown in bold in Table 1). The PMT voltages were then varied ±20 V from the gain-matched condition to assess the resulting variation of the combined ROI count rate relative to the reference.

The results in Table 1 show that the neutron count rate varied by only a fraction of a percent when adjusting the PMT high voltages by ±20 V. This stability of the neutron count rate in response to high-voltage changes demonstrates the reliability of the ^{6}Li glass composite scintillator detector's neutron counting performance. This characteristic is crucial to ensure accurate measurements over extended durations. Furthermore, this behavior resembles that of ^{3}He proportional neutron detectors operating in the so-called high voltage plateau, where the neutron count rate remains

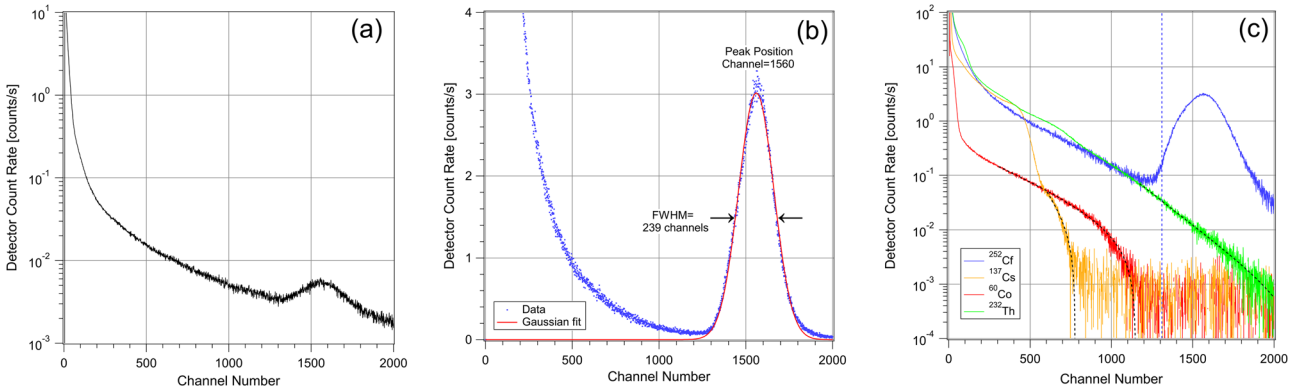

Fig. 3 | Pulse-height spectra recorded for various radiation sources. a Pulse-height spectrum of the natural background (no sources present) recorded at Los Alamos National Laboratory (elevation 2198 m above sea level) for a measurement duration of 49089 s; this background was subtracted from all raw pulse-height distributions measured for sources present (**b** and **c**). **b** Pulse height spectrum (blue dots) measured using irradiation with a 10.5 μCi ^{252}Cf fission neutron source (measurement duration 600 s). The solid red line is a least-squares fit of a Gaussian function to the neutron capture peak using the data in the 1310–2000 channel range. The peak is at channel 1560 with a full width at half maximum (FWHM) of 239 channels, yielding an energy resolution of 15.3%. **c** Pulse height spectra due to gamma were measured using irradiation with ^{137}Cs (orange dots, measurement duration 4006 s), ^{60}Co (red dots, measurement duration 7981 s), and ^{232}Th (green dots, measurement duration 6000 s) gamma sources. The count rates are shown on a log-scale. The pulse height spectrum from Fig. 3b is shown for reference (blue dots). The channel 1310–2000 region of interest (ROI) is indicated by a dashed blue vertical line. The dashed black lines are double exponential fits to the Compton tails of the respective pulse-height spectra.

practically independent of the high voltage variation (within a limited specific range of operating voltage)[5].

Cross calibration and dynamic range. Figures 4a and b show the combined count rate and combined current from both PMTs of the ^{6}Li glass composite scintillator detector, respectively, measured at various neutron fluxes. The variation in the neutron flux was achieved by positioning the detector at various distances ranging from 50 to 230 cm from the ^{252}Cf source (emitting 5.2×10^{8} n/s) located at the neutron-free-in-air (NFIA) facility at the Central Health Physics Calibration Facility (CHPCF at Los Alamos National Laboratory, TA-36). The neutron count rate was found to depend linearly on the neutron flux up to ~2.6×10^{3} n/(s·cm^{2}), corresponding to a count rate of ~3×10^{4} cps (see Fig. 4a). Deviation from linear behavior was observed for greater neutron flux, as the dead time correction processing in the multi-channel analyzer (Ortec 927 ASPEC) became increasingly inaccurate for dead time fractions greater than 25%. The Ortec 927 implements the Gedcke-Hale extended live-time method for dead time correction[23]. This method may underestimate or overestimate the true count rate when the pulse pileup rate is too high. In contrast, the PMT current depended linearly on all neutron fluxes measured in this experiment (see Fig. 4b).

The range of neutron fluxes <2.6×10^{3} n/(s·cm^{2}) defines a cross-calibration regime in which the neutron count rate is not yet saturated (Fig. 4a) and a PMT current can be measured (Fig. 4b). Using this data, Fig. 5a plots the PMT current *vs* the neutron count rate in this cross-calibration regime. The linear fit represents an approximation for the charge per neutron capture event produced by the PMTs, allowing the current to be cross-calibrated to the count rate. A cross-calibration constant of 78.5 pC per neutron capture was found, a value characteristic of this particular detector configuration. Note that this approach tends to overestimate the charge per neutron capture event because the PMT current results from all interactions that generate scintillation light (neutron and gamma), while the count rate in the ROI is almost exclusively due to neutron capture events. Being cognizant of this limitation, the cross-calibration constant was then used to convert the current measurements into neutron count rates, revealing the wide dynamic range of the ^{6}Li glass composite scintillator detector. As shown in Fig. 5b, the detector response in current mode was found to be linear over a dynamic range extending from single event neutron counting at background levels up to the maximum total incident neutron flux of 3.7×10^{6} n/s that was achievable at the NFIA facility.

Table 1 | Sensitivity of the detector count rate to the variation of the high voltages applied to the photomultipliers (PMTs)

		PMT B		
		963 V	**983 V**	**1003 V**
PMT A	**980 V**	96.96%	99.12%	99.86%
	1000 V	99.59%	100.00%	100.49%
	1020 V	99.44%	100.34%	100.17%

The detector count rates for various PMT voltage settings are given as percentages of the detector count rate measured for the nominal operating voltages of 1000 V (PMT A) and 983 V (PMT B).

Neutron detection efficiency. The neutron detection efficiency is defined as the number of neutrons detected in the ROI per the number of neutrons incident upon the detector. With reference to fission (fast) neutrons, it was evaluated both experimentally (^{252}Cf fission source) and compared with Monte Carlo simulations. The slope of the linear fit in Fig. 5b corresponds to the experimentally determined intrinsic neutron capture efficiency, and a value of 6.70 ± 0.01% was found.

Additionally, Monte Carlo N-Particle (MCNP 6.2) simulations, with the Evaluated Nuclear Data File (ENDF) VIII library, were performed, assuming the National Institute of Standards and Technology (NIST) calibrated ^{252}Cf neutron source was located 2.3 meters from the center of the detector, perpendicular to the detector axis[24,25]. In the MCNP code, the ^{6}Li glass particle/mineral oil composite prototype was simulated with the same detector geometry as described in the Fabrication Section. The detector model was integrated into a high-fidelity validated model of the NFIA facility (see Methods section). Simulations of the experiment were performed using an isotropic ^{252}Cf source and the full NFIA facility geometry to accurately capture the effects of scattering in the room. The intrinsic neutron capture efficiency was calculated from simulations as the ratio of the number of captures to the number of incident neutrons on the detector, yielding a value of to be 7.3 ± 0.2%. The error was determined by propagating the statistical errors in the number of captures (3.7×10^{10} histories) and in the incident neutron flux.

Die-away time. The die-away time of the detector was measured using the Rossi-α method[5,9], which records the time distribution of neutron events following every detected neutron on the pulse train chosen as the initiating neutron event. The Rossi-α distribution is constructed by

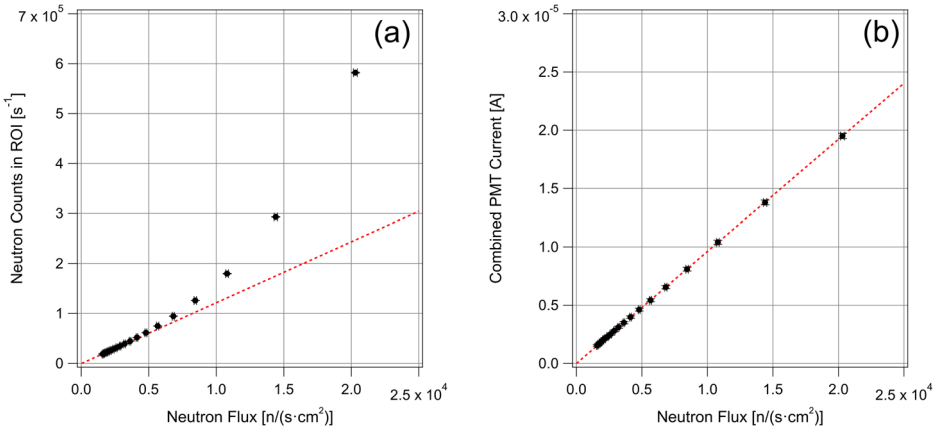

Fig. 4 | Photomultiplier (PMT) count and current signals under high-intensity ^{252}Cf irradiation. **a** Combined (PMT A + PMT B) neutron count rate in the region of interest (ROI) for various neutron fluxes. The red dashed line is a linear fit to the data up to a neutron flux of 2.6×10^3 n/(s·cm^2). **b** Combined (PMT A + PMT B) PMT current for various neutron fluxes. The red dashed line is a linear fit to the full data set with the y-axis intercept set to zero. It yielded a slope of 9.611×10^{-10} C·cm^2/n with $R^2 = 0.999986$. The error bars in both figures represent the ±1 standard deviation of the statistical measurement uncertainty.

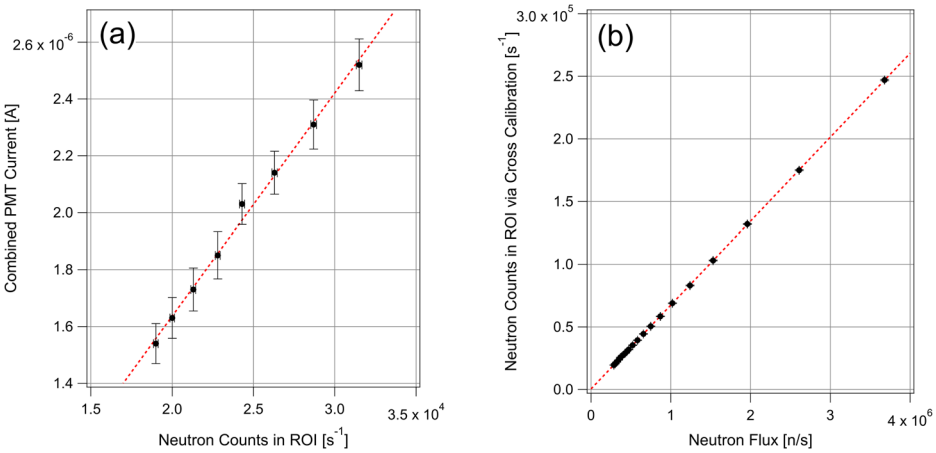

Fig. 5 | Cross calibration of the ^{6}Li glass composite scintillator detector. **a** PMT current *vs* neutron count rate in the region of interest (ROI) using the data shown in Fig. 4 for neutron fluxes of $<2.6 \times 10^3$ n/(s·cm^2). The slope of the linear fit (red dashed line) corresponds to the charge per neutron capture event produced by the PMTs, and this cross-calibration constant was found to be 78.5 pC ($R^2 = 0.9950$) per neutron capture for this detector configuration. **b** PMT current (from Fig. 4b) converted to neutron count rates using the above cross-calibration constant *vs* the total neutron flux on the detector, assuming a lateral surface area of 181.22 cm^2. The slope of the linear fit (red dashed line) corresponds to the neutron detection efficiency and was found to be 6.70 ± 0.01% ($R^2 = 0.99999$). The error bars in both figures represent the ±1 standard deviation of the statistical measurement uncertainty.

recording the time interval between subsequent neutron events within a specified time window. The process involves moving to the next neutron event trigger and repeating the acquisition of the arrival time distribution[5]. Fig. 6a shows the detector die-away time response measured using the Rossi-α method. The constant background due to uncorrelated neutron detection events was subtracted for clarity. The rise of the transient at $t < 2$ μs is due to the 2 μs dead time of the multichannel analyzer. The transient exhibits a fast component at early times (2 μs < t < 8 μs), while at longer times (t > 8 μs), the behavior is dominated by thermal neutron diffusion, and the decay is single exponential. The red dashed line is a single exponential fit to the data in the 8–60 μs range, yielding a decay time of 10.3 ± 0.1 μs.

As for the efficiency, MCNP Monte Carlo simulations were performed to estimate the neutron die-away time[25], and the results are presented in Fig. 6b. The time distribution was fitted with a simple exponential model within the 8–60 μs range to determine the detector's die-away time, and a value of 10.21 ± 0.16 μs was found. This aligns closely with the experimental value of 10.3 ± 0.1 μs.

The die-away time is dominated by thermal neutron diffusion through the mineral oil moderator to the ^{6}Li glass scintillator cubes. The high density of ^{6}Li neutron capture centers throughout the moderator leads to a shorter average diffusion path compared to a detector consisting of ^{3}He tubes encased in polyethylene. Thus, the die-away time in the composite detector is shorter than the several tens of μs die-away time that is typical of ^{3}He proportional counter-based systems embedded in polyethylene. This characteristic is crucial as it minimizes the impact of accidental coincidence in neutron coincidence/multiplicity type detector systems (see Discussion section of the paper)[9,10].

Position sensitivity of the neutron flux interaction. Scintillation light experiences some attenuation as it propagates through the composite. If a neutron capture event occurs in the middle between the two PMTs, the resulting scintillation light is attenuated equally as it propagates the same distance, on average, to each of the PMTs, and the pulse heights registered by the PMTs are, on average, equal. If, however, the neutron capture event occurs closer to PMT A than to PMT B, then the resulting scintillation light is attenuated less on its shorter path to PMT A, and the pulse height registered by PMT A is thus greater than that registered by PMT B. This effect can be utilized to detect the location of neutron capture events along the composite cylinder's long axis.

Figure 7 shows the change in the pulse-height spectra recorded by PMT A (red curves) and PMT B (green curves) for a ^{252}Cf source placed at five different positions along the long axis of the composite cylinder, with $z = 0$, indicating the center of the composite cylinder. The pulse-height spectra recorded for uniform illumination of the detector are also shown for reference. Each pulse-height spectrum contained 10^5 neutron capture events. Note that the pulse-height spectra shown here are for the individual PMTs, and the pulse-height resolution is, therefore, significantly worse than that shown in Figs. 1 and 3, which used the combined PMT A and PMT B signals. As expected, the individual pulse-height spectra of PMT A and PMT B for the symmetrical case of $z = 0$ were found to be identical as the scintillation light propagation losses from the center to PMT A and from the center to PMT B are identical. A symmetric case was also realized for uniform neutron illumination, resulting in identical pulse-height spectra for PMT A and PMT B. In contrast, the pulse-height spectra deviated as the source was moved away from the center of the composite cylinder, and the respective light propagation losses became different. As expected, the

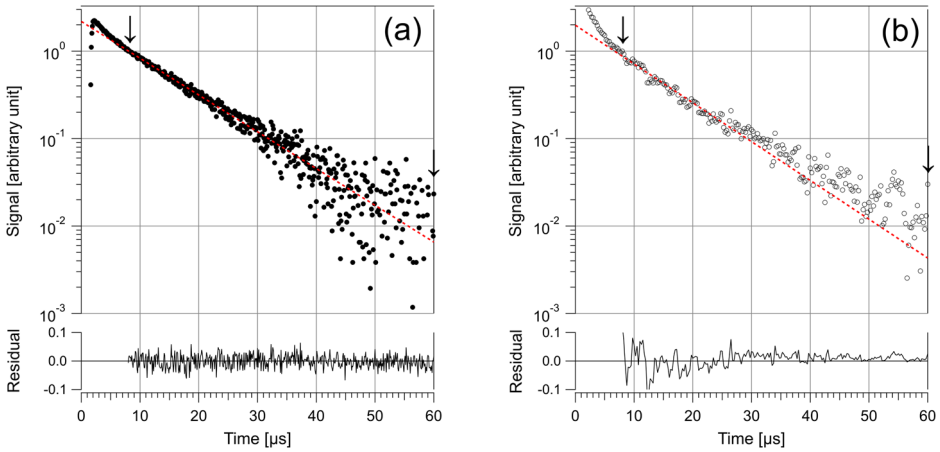

Fig. 6 | Die-away time of the ^{6}Li glass composite scintillator detector. a Top panel: Detector die-away transient measured using the Rossi-α method, where the constant background of the Rossi-α distribution has been subtracted for clarity (solid circles). The red dashed line is a single exponential fit to the data in the range 8–60 μs (as indicated by arrows), and it yielded a decay time of 10.3 ± 0.1 μs. Bottom panel: Residual between the measured data and the fit. **b** Top panel: Die-away transient calculated using MCNP (open circles). The red dashed line is a single exponential fit to the data in the range 8–60 μs (as indicated by arrows), and it yielded a decay time of 10.21 ± 0.16 μs. Bottom panel: Residual between the calculated MCNP data and the fit. Plots (a) and (b) were normalized to 1 at 8 μs.

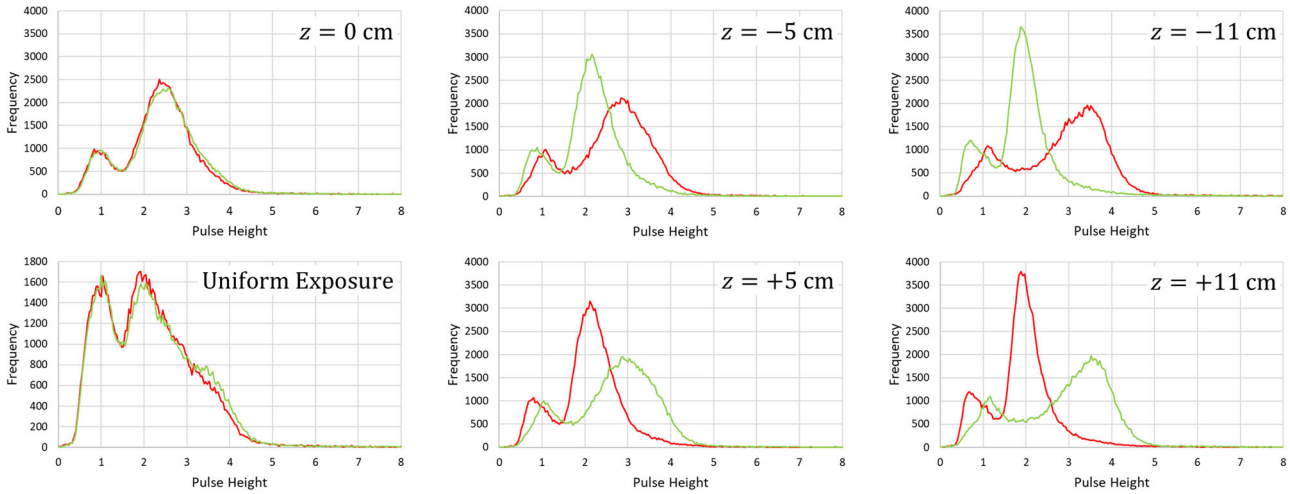

Fig. 7 | Pulse-height spectra for irradiating the ^{6}Li glass composite scintillator detector at different positions along the composite. Pulse-height spectra recorded by photomultiplier (PMT) A (red curves) and PMT B (green curves) for a ^{252}Cf source placed at five different positions along the long axis of the composite cylinder, with $z = 0$ indicating the geometric center of the composite cylinder. The pulse-height spectra recorded for uniform neutron exposure of the detector are also shown for reference. Note that, because the PMT outputs were not summed but rather read out individually, the pulse-height spectra shown here have lower resolution compared to the pulse-height spectra shown in Figs. 1 and 3a, where the output of the two PMTs were summed.

changes were found to be anti-symmetrical in that the pulse-height spectra for $z = \pm 5$ cm and for $z = \pm 11$ cm they were identical except for PMT A and PMT B being reversed.

We define the dispersion variable

$$\xi = \frac{A - B}{A + B} \tag{1}$$

where A and B are the background-corrected pulse heights registered in PMT A and PMT B for a single neutron capture event. For each source position, a histogram of 10^5 single-event ξ values [Eq.(1)] was calculated, and a normal distribution was fit to the histogram to obtain the mean dispersion variable, $\bar{\xi}$. Figure 8 plots the ^{252}Cf source positions, z, versus the respective $\bar{\xi}$. As indicated by the least squares fit $z = a\bar{\xi} + b$, there is a strong linear relationship ($R^2 = 0.9934$) between z and $\bar{\xi}$. From the standard errors in a and b (see inset in Fig. 8), we calculate the 1σ error in the predicted ^{252}Cf source position to be $\sigma_z = \pm 0.36$ cm for the source located in the center along the composite ($z = 0$ cm) and $\sigma_z = \pm 0.61$ cm for the source located at either end ($z = \pm 11$ cm) of the composite. This position sensitivity may be attractive for applications requiring precise spatial information in neutron detection, such as nuclear security (e.g., verification at ports)[7] and neutron radiography.

Discussion

The performance of neutron multiplicity counting relies on crucial factors, including neutron detection efficiency, die-away time, sensitivity to gamma rays, count rate capability, and counting stability during extended measurements. To assess the performance of the present ^{6}Li-glass particle detector for a proposed use in neutron multiplicity counting, we conducted initial Monte Carlo simulations using the MCNP 6.2 code. The results of the previous sections demonstrate that MCNP simulations can effectively replicate the detector's performance. The MCNP simulations involved filling a counter with ^{6}Li-glass-composite material, mimicking the form factor of the widely used Active Well Coincidence Counter (AWCC)[5] – a typical system used in nuclear safeguards based on ^{3}He counters embedded in high-density polyethylene. The modeling assumed uniformly distributed 1 mm^3 lithium glass particles with a 4 mm pitch. While light transport was not considered, the calculation estimated the neutron reaction rate. Additionally, different from the original AWCC based on ^{3}He, detection material was filled in the well's top and bottom end plugs, enabling a detector solid angle of approximately 4π. This is a possibility which was impracticable with the traditional ^{3}He-based neutron counter. The results of the Monte Carlo simulations revealed impressive performance improvements for the AWCC-^{6}Li-composite-based detector. It exhibited approximately 2.5 times higher absolute efficiency (ε) and around 3.6 times shorter die-away time (τ)

compared to the ^{3}He-based AWCC. This achievement brought the performance of the ^{6}Li-glass-particle-based AWCC on par with the exemplary characteristics of the Epithermal Neutron Multiplicity Counter (ENMC)[26] but with a significantly reduced footprint. The performance metric, often expressed as Figure-of-Merit (FOM) for multiplicity neutron detectors, can be represented by the equation FOM $= \varepsilon/\sqrt{\tau}$. A higher FOM corresponds to better multiplicity detector performance[11,14]. Results are presented in Table 2. For reference, the ENMC boasts a FOM of 13.9, while the simulated ^{6}Li-glass-particle-based AWCC demonstrated an impressive theoretical FOM of 17.6. Even considering the loss due to light transport, the simulation results suggest that our design outperforms ^{3}He-based multiplicity systems. In addition, the performance calculated so far assumes a "point" item at the center of the cavity. Note that the position-sensitive characteristic of the ^{6}Li composite detector may provide further information related to the distribution of the nuclear material in the item under analysis. These findings promise to advance neutron multiplicity counting capabilities in various scientific and nuclear security applications.

The detection of shielded nuclear material in nonproliferation and safeguards applications has seen advancements through active interrogation techniques, which involve using intense neutron pulses to interrogate the presence of nuclear material, particularly uranium items[27]. Recent developments in laser-driven pulse neutron sources have showcased the production of highly intense, pulse-forward neutron beams, opening the door to a new generation of active interrogation systems[28,29]. Neutron yields on the order of more than 10^{10} neutrons per sr per pulse have been demonstrated with about 80 J laser energy, in a conversion two-step approach where laser light impinging on a suitable target produced a burst of ions that are converted in material such as Be or Li. A pulse of fast neutrons with a distribution of several MeV is produced in a few ns. These laser-driven neutron sources for applications in global security systems demand high-performance neutron detectors in terms of efficiency and dynamic range to measure induced neutrons[28–31]. In this context, the ^{6}Li-glass particle detector offers advantages over traditional ^{3}He detector systems for such applications.

The compactness and modularity of the present ^{6}Li glass particle detection system are essential features. They are particularly valuable for nuclear security and emergency applications, where portability is crucial. In such cases, Silicon Photomultipliers (SiPMs) can be utilized instead of Photomultiplier Tubes (PMTs) to ensure even greater compactness with a weight reduction. In addition, the form factor (e.g., square size for the detectors) can be selected to facilitate modularity and portability, where several detector modules can be easily arranged to assemble a coincidence/multiplicity counter directly in the field. The neutron detection technology presented in this study holds significant promise for enhancing active interrogation capabilities and addressing nuclear security challenges. Additionally, ^{6}Li-glass scintillator composite detectors can play a crucial role in fundamental science. For instance, these detectors can find applications in pulsed neutron measurements around large-scale accelerators and TRIGA burst reactors[32,33], in measurements of β-delayed neutron emission[34–38], in neutrino experiments[39], and in measurements of cross-sections[40]. Finally, we mention here that we have been developing a solid version of the detector in a separate effort. This solid version is intended for applications where an oil-filled detector may not be suitable.

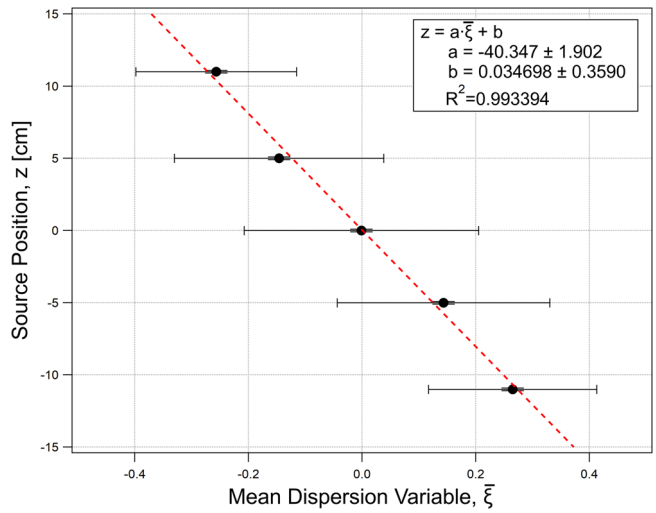

Fig. 8 | Position sensitivity of the ^{6}Li glass composite scintillator detector. As indicated by the least-squares linear fit (dashed red line), there is a strong linear relationship ($R^2 = 0.9934$) between the ^{252}Cf source position, z, and the mean dispersion variable, $\bar{\xi}$. The respective fit parameters are shown in the inset. The source position error is ±0.1 cm, and the error bar shown for $\bar{\xi}$ corresponds to the ±1σ width of the Gaussian distribution obtained from a least-squares fit to the respective histogram of 10^5 single-event ξ values.

Methods

Detector fabrication

A GS20^{TM} ^{6}Li glass scintillator plate (Scintacor, Cambridge, UK), with dimensions of 158 mm × 158 mm × 1.5 mm and polished to an optical finish on each side, was diced into 1.5 mm × 1.5 mm × 1.5 mm cubes using a diamond cutting wheel. The resulting cubes had two opposing polished faces and four as-diced rougher faces. Next, UV-curable NOA88 optical adhesive (Norland Products, Cranbury, NJ) was used to glue the ^{6}Li glass scintillator cubes to the outer surfaces of fused silica tubes having a cross-section of 2.7 mm × 2.7 mm, a wall thickness of 0.35 mm, and a length of 256.8 mm (Technical Glass Products, Inc., Painesville Twp., OH). 50 scintillator cubes were affixed with a center-to-center spacing of 4.7 mm to each lateral side of the square tubes, using the as-diced sides of the cubes as a gluing interface. The linear array was offset by 2.35 mm on adjacent sides of the square tube. A total of 8200 GS20 scintillator cubes were used to fabricate 41 such scintillating tube assemblies. A hexagonal pattern (7.24 mm lattice constant) of 45 holes (4.0 mm diameter) was drilled into two 4.0 mm thick and 65 mm diameter disks of Solacryl® SUVT acrylic (Spartech Polycast, Maryland Heights, MO). These two disks and four square fused silica tubes (without GS20 cubes) were used to create a structure to support the

Table 2 | Comparison of neutron multiplicity counter performances

Characteristic	AWCC (^{3}He)	ENMC (^{3}He)	AWCC (^{6}Li particle-based 4-mm pitch)
Outer dimension [cm]	48 (diameter)	66 (per side, box geometry)	48 (diameter)
Weight (estimated) [kg]	84	280	122
Neutron detection efficiency (fission/fast neutrons) with item in the center of the cavity	26%	65%	66%
Die-away time [μs]	51	22	14
Multiplicity. FOM $= \varepsilon/\sqrt{\tau}$ [(%)/(μs$^{1/2}$)]	3.6	13.9	17.6

The table compares the performance of the existing ^{3}He-based Active Well Coincidence Counter (AWCC) and Epithermal Neutron Multiplicity Counter (ENMC) with that of a modeled ^{6}Li particle-based AWCC.

41 scintillating tube assemblies that were inserted through the holes in the acrylic disks.

This assembly was then inserted into a fused silica tube of 69.7 mm internal diameter, 2.25 mm wall thickness, and 260 mm length (Technical Glass Products, Inc., Painesville Twp., OH), which also had two tubular ports at each end of the lateral surface. This assembly defined the active volume of the prototype built.

Next, the windows of two Hamamatsu R6233 photomultiplier tubes were glued to each open end of the fused silica tube containing the scintillator rod assembly. This produced a liquid-tight cylindrical container that was then filled with Drakeol®9LT (Calumet Specialty Product Partners, Karns City, PA) mineral oil through the two tubular ports, thus completely submersing the scintillating tube assembly in mineral oil. After sealing the tubular ports, a 250-μm diameter silica optical fiber was spiral-wound (7 windings) around the length of the fused silica tube to create an air gap for the subsequent wrapping with Vikuiti™ Enhanced Specular Reflector (ESR) film (3M Company, Maplewood, MN). The air gap ensured that scintillation light emitted within the assembly and incident on the lateral surface of the fused silica tube with an angle greater than the angle of total internal reflectance (TIR) would undergo lossless TIR rather than lossy reflection at the ESR film. The latter only interacted with the fraction of light that did not undergo TIR and escaped from the fused silica tube assembly. Finally, a 0.5-mm thick cadmium sheet was wrapped around the outside of the assembly to prevent any thermal neutrons from entering the detector through the lateral surface. This comprehensive fabrication process successfully created the oil-based scintillating detector, a picture of which is shown in Fig. 2.

Pulse height spectra measurement setup

Pulse height spectra were recorded by summing the outputs from the anodes of the two PMTs and conditioning it with an in-house charge-sensitive preamplifier with a sensitivity of 10 mV/pC and a decay constant of 200 μs, followed by an Ortec 672 shaping amplifier set to a gain of 34 and a shaping time constant of 1.5 μs. The processed signal pulses were then analyzed using an Ortec 927 ASPEC multi-channel analyzer (MCA). Data acquisition was performed with the Ortec Maestro software. The voltages of PMT A and PMT B were adjusted to 1000 V and 983 V, respectively, to match the respective positions of the ^{6}Li neutron capture peak in the pulse-height histograms, thus ensuring equal gain of the two PMT/pre-amplifier chains.

Die-away time measurement setup

To measure the time distribution of neutron detection events, the PMT outputs from both sides were fed into a chain consisting of a preamplifier, Ortec 672 shaper/amplifier, followed by an Ortec 551 timing Single Channel Analyzer (SCA). The SCA threshold was adjusted only to include the neutron peak from the system's pulse height spectrum. The arrival times of the pulses were then recorded using a pulse train recorder[34].

Position sensitivity measurement setup

To assess the position sensitivity capability of the composite detector, we conducted experiments using a ^{252}Cf fission neutron source mounted inside a 2-inch (5.08 cm) diameter and 4-inch (10.16 cm) long cylindrical tungsten cylinder that had a 3/8 inch (0.9525 cm) opening through the center. The source was pushed to one side of the tungsten holder and placed in direct contact with the detector. This source assembly was placed at various positions along the lateral surface of the composite detector to measure its position sensitivity. The signals from the PMTs on each side were connected to independent preamplifiers and shaper channels (not summed) with the same parameters as described in the Pulse Height Measurement Setup section. The high voltages of both PMTs remained as described in the Pulse Height Measurement Setup configuration to preserve the gain matching. The pulses from each side were recorded in coincidence using a digital oscilloscope. To calculate a residual metric, 10^5 electrical pulses were accumulated at each spatial position.

Cross calibration and dynamic range measurements setup

A series of experiments were conducted at the Central Health Physics Calibration Facility (CHPCF at Los Alamos National Laboratory, TA-36) in the neutron-free-in-air (NFIA) facility, which is designed to reduce undesired neutron scattering by the experimental hall. A ^{252}Cf fission neutron source with a NIST (National Institute of Standards and Technology) traceable calibration was used. To obtain the total neutron flux [neutrons/(s·cm^2)] at the various ^{6}Li glass composite scintillator detector distances from the ^{252}Cf source, both direct and scattered contributions were calculated using MCNP6.2 coupled with the ENDF VIII library (see section Reference measurements and neutron flux at the Central Health Physics Calibration Facility).

Reference measurements and neutron flux at the Central Health Physics Calibration Facility

The Central Health Physics Calibration Facility (CHPCF) is a secondary standards laboratory at LANL that maintains several neutron, gamma, and beta reference fields for the routine calibration of health physics instruments. These fields are also made available for special studies by researchers both within and outside the Laboratory.

As a secondary standards lab, all reference fields at the CHPCF are traceable to a national or international standard. Of interest to this study is the neutron-free-in-air (NFIA) reference field located inside a large hall (12 m × 12 m × 7 m). The neutron sources (^{252}Cf) are stored below grade and raised pneumatically from a control console outside the hall. The sources are raised about 4 m above the concrete floor to a low-scatter aluminum platform upon which sits the irradiator assembly. A linear positioning stage (LPS) located on the platform allows precise positioning of instruments with respect to the irradiator. Positioning of the LPS at distances ranging from 30-300 cm from the source is also done remotely from the control console. Instruments placed on the LPS are aligned vertically and horizontally using lasers. The wall directly behind (and nearest) the irradiator is made of drywall to minimize scattering. The remaining walls in the hall are constructed of concrete.

The NFIA sources are calibrated at NIST (National Institute of Standards and Technology) with respect to 4π emission rate using a Mn-bath technique with typical uncertainties on the order of 1.6% (k = 1). MCNP6.2, coupled with ENDF VIII cross-section library, was used for calculations of neutron fluence based on a comprehensive model of the NFIA facility (including the source and irradiator construction) normalized per source neutron to provide the neutron (spectral) flux. These MCNP-calculated quantities were then scaled based on the NIST-calibrated emission rate. The irradiator software at the control console automatically applies a decay-corrected dose rate for each source and distance daily.

For the purposes of the performance evaluation of the ^{6}Li-composite-based detector, the direct and scattered contributions to neutron fluence at selected distances from a neutron source were calculated using MCNP6.2 as described before, but this time considered the source term to be comprised of not only the doubly encapsulated source but also the aluminum rabbit and the immediate environs of the irradiator assembly. The rest of the hall was modeled as a void, and point detector tallies (F5 type, detector fluence in neutron/cm^2 [24,25]) at distances of interest were used to determine the "direct" fluence based on the total F5 tally score. Subtracting these results from those based on the earlier comprehensive model gave the combined contribution of room and air scatter to the total fluence and dose. The least squares fit of the "direct" fluence showed a $1/d^2$ dependence for distances ranging from 30 to 300 cm, as expected for a point-like source as it is a ^{252}Cf fission neutron source. When calculated in this fashion, the "direct" fluence was 10% higher in the horizontal (i.e. the instrument) plane than based on just the bare source 4π emission rate. This increase was partly due to the inherent anisotropy of the cylindrical source capsule (~ 2% effect) supplemented by scatter within the extended source term. Measurements using neutron spectrometers such as Bonner spheres and ROSPEC have validated the

dose rates derived using the approach described above. A detailed uncertainty budget analysis for the NFIA indicated typical total uncertainties on the fluence of ±6.0% for the NFIA ^{252}Cf sources (k = 2).

Data availability

All data generated and analyzed during the current study are presented here. Raw data can be available from the corresponding authors upon reasonable request.

Received: 9 March 2024; Accepted: 4 December 2024;
Published online: 04 January 2025

References

1. Byrne, J. *Neutrons, Nuclei and Matter: an exploration of the physics of slow neutrons* (Dover Publications, 2013).
2. Segre, E. *Nuclei and Particles: An introduction to Nuclear and Subnuclear physics*. (Benjnamin-Cummings Pub Co., 1978).
3. Beckhurts, K. H. & Wirtz, K. *Neutron Physics*. (Springer, 1964).
4. Knoll, G. F. *Radiation Detection and Measurement*. (John Wiley & Sons Inc., 2010).
5. Reilly, D., Ensslin, N., Smith, H., Jr. & Kreiner, S. (Eds). Passive Nondestructive assay of nuclear materials. US Nuclear Regulatory Commission report NUREG/CR-5550. Los Alamos National Laboratory report LA-UR-90-732. (1991).
6. Neutrons for the Nation. Discovery and Applications while Minimizing the Risk of Nuclear Proliferation. A Report by the American Physical Society on Public Affairs. *APS Physics*, https://www.aps.org/policy/reports/popa-reports/upload/APSNeutronsfortheNation.pdf (2018).
7. Cho, O. Helium-3 shortage could put freeze on low-temperature research. *Science* **326**, 778–779 (2009).
8. Sacchetti, F. et al. ^{3}He-free neutron detectors and their applications. *Eur. Phys. J.* **130**, 53 (2015).
9. Croft, S., Favalli, A., Hauck, D. K., Henzlova, D. & Santi, P. A. Feynman variance-to-mean in the context of passive neutron coincidence counting. *Nucl. Instrum. Methods Phys. Res. A* **686**, 136–144 (2012).
10. Favalli, A., Croft, S. & Santi, P. Point model equations for neutron correlation counting: Extension of Böhnel's equations to any order. *Nucl. Instrum. Methods Phys. Res. A* **795**, 370–375 (2015).
11. Henzlova, D. et al. Current status of Helium-3 alternative technologies for nuclear safeguards. U.S. DOE, Los Alamos National Laboratory report (LA-UR-15-21201) (2015).
12. Kouzes, R. T. et al. Neutron detection alternatives to ^{3}He for national security applications. *Nucl. Instrum. Methods Phys. Res. A* **623**, 1035–1045 (2010).
13. Peerani, P. et al. Testing on novel neutron detectors as an alternative to ^{3}He for security applications. *Nucl. Instrum. Methods Phys. Res. A* **696**, 110–120 (2012).
14. Lintereur, A. T. et al. Alternatives to Helium-3 for neutron multiplicity counters. *2012 IEEE Nuclear Science Symposium and Medical Imaging Conference Record (NSS/MIC)*, Anaheim, CA, USA, 547–553, (2012).
15. Ianakiev, K. D., Swinhoe, M. T., Favalli, A., Chung, K. & MacArthur, D. W. ^{6}Li foil scintillation sandwich thermal neutron detector. *Nucl. Instrum. Methods Phys. Res. A* **652**, 417–420 (2011).
16. Ianakiev, K. D. et al. Neutron detector based on Particles of ^{6}Li glass scintillator dispersed in an organic lightguide matrix. *Nucl. Instrum. Methods Phys. Res. A* **784**, 189–193 (2015).
17. Hehlen, M. P., Wiggins, B. W., Favalli, A., Iliev, M. & Ianakiev, K. D. Light propagation in a neutron detector based on ^{6}Li glass scintillator particles in an organic matrix. *J. Appl. Phys.* **124**, 124502 (2018).
18. Wiggins, B. W., Favalli, A., Iliev, M., Ianakiev, K. D. & Hehlen, M. P. Computational investigation of arranged scintillating particle composites for fast neutron detection. *Nucl. Instrum. Methods Phys. Res. A* **915**, 17–23 (2019).
19. Dazeley, S., Asghari, A., Bernstein, A., Bowden, N. S. & Mozin, V. A. Water-based neutron detector as a well multiplicity counter. *Nucl. Instrum. Methods Phys. Res. A* **771**, 32–38 (2015).
20. McGregor, D. S., Klann, R. T., Gersch, H. K. & Yang, Y. H. Thin-film-coated bulk GaAs detectors for thermal and fast neutron measurements. *Nucl. Instrum. Methods Phys. Res. A* **466**, 126–141 (2001).
21. https://scintacor.com/products/6-lithium-glass/ last accessed October 14th, 2023.
22. Favalli, A., Iliev, M., Ianakiev, K., Hunt, A. W. & Ludewigt, B. Delayed gamma-ray spectroscopy with lanthanum bromide detector for non-destructive assay of nuclear material. *Nucl. Instrum. Methods Phys. Res. A* **877**, 192–196 (2018).
23. Jenkins, R., Gould, R. W. & Gedcke, D. *Quantitative X-Ray Spectrometry* 266–267 (Marcel Dekker, Inc., New York, 1981).
24. Kulesza, J. A. et al. MCNP® Code Version 6.3.0 Theory & User Manual. Los Alamos National Laboratory Tech. Rep. LA-UR-22-30006, Rev. 1. Los Alamos, NM, USA. (2022).
25. Hendricks, J. S., Swinhoe, M. T., Favalli, A. Monte Carlo N-Particle Simulations for Nuclear Detection and Safeguards. Springer (2022).
26. Menlove, H. O., Rael, C. D., Kroncke, K. E. & DeAguero, K. J. (2004). Manual for the Epithermal Neutron Multiplicity Detector (ENMC) for Measurement of Impure MOX and Plutonium Samples. Los Alamos National Laboratory, USA.
27. Favalli, A., Mehner, H.-C., Crochemore, J.-M. & Pedersen, B. Pulsed neutron facility for research in illicit trafficking and nuclear safeguards. *IEEE Trans. Nuc. Sci.* **56**, 1292–1296 (2009).
28. Favalli, A. et al. Characterizing laser-plasma ion accelerators driving an intense neutron beam via nuclear signatures. *Sci. Rep.* **9**, 2004 (2019).
29. Favalli, A. et al. Laser-driven neutron source for detection of nuclear material. In *Proc. 2016 Advances in Nuclear Nonproliferation Technology and Policy Conference*, Santa Fe, NM, USA (2016).
30. Huang, C. K. et al. High-yield and high-angular-fluence neutron generation from deuterons accelerated by laser-driven collisionless shock. *Appl. Phys. Lett.* **120**, 024102 (2022).
31. Roth, M. et al. Bright laser-driven neutron sources based on relativistic transparency of solids. *Phys. Rev. Lett.* **110**, 044802 (2013).
32. Taylor, A. et al. Route to the brightest possible neutron source. *Science* **315**, 1092–1095 (2007).
33. Shabalin, E. P. *Fast pulsed and burst reactors* (Pergamon, 2013).
34. https://www.iki.kfki.hu/radsec/research/PTR-32_ThrowAway2.pdf (last access, Sept. 27, 2024).
35. Pereira, J. et al. The neutron long counter NERO for studies of β-delayed neutron emission in the r-process. *Nucl. Instrum. Methods Phys. Res. A* **618**, 275–283 (2010).
36. Grzywacz, R. et al. Hybrid-3Hen – New detector for gammas and neutrons. *Acta Phys. Pol. B* **45**, 217–222 (2014).
37. Tolosa-Delgado, A. et al. Commissioning of the BRIKEN detector for the measurement of very exotic β-delayed neutron emitters. *Nucl. Instrum. Methods Phys. Res. A* **925**, 133–147 (2019).
38. Kratz, K.-L. Relevance of β-delayed neutron data for reactor, nuclear physics and astrophysics applications. *Eur. Phys. J. A* **59**, 99 (2023).
39. Amsbaugh, J. F. et al. An array of low-background ^{3}He proportional counters for the Sudbury Neutrino Observatory. *Nucl. Instrum. Methods Phys. Res. A* **579**, 1054–1080 (2007).
40. Clisu, C. et al. Cross section measurements of low-energy charged particle induced reactions using moderated neutron counter arrays. *EPJ Web Conf.* **284**, 01015 (2023).

Acknowledgements

The research presented in this article was supported by the Laboratory Directed Research and Development program of Los Alamos National

Laboratory under project number 20210431ER. We acknowledge the support received from N. Wehmann, C. Roybal, J. Bland, J. Mendez, M. Olivas, D. Jones, R. Weinmann-Smith, and M. Swinhoe. We acknowledge insightful discussions with Prof. S. Croft, Lancaster University.

Author contributions

A.F.: concept, methodology, and analysis; B.W.W., C.G.R., K.O., T.D.M.: experiments and analysis; M.I.: experiments and electronics; K.D.I.: concept and electronics; M.P.H. concept, analysis, and supervised the project. A.F. and M.P.H. wrote the manuscript with contributions from all the authors.

Competing interests

The authors declare no competing interests.

Additional information

Supplementary information The online version contains supplementary material available at https://doi.org/10.1038/s42005-024-01903-3.

Correspondence and requests for materials should be addressed to Andrea Favalli or Markus P. Hehlen.

Peer review information *Communications Physics* thanks Richard Kouzes and the other, anonymous, reviewer(s) for their contribution to the peer review of this work. A peer review file is available.